

Electrical Control of Surface Acoustic Waves

Linbo Shao,^{1,*} Di Zhu,¹ Marco Colangelo,² Dae Hun Lee,³ Neil Sinclair,^{1,4} Yaowen Hu,^{1,5} Peter T. Rakich,⁶ Keji Lai,³ Karl K. Berggren,² and Marko Lončar,^{1,†}

¹*John A. Paulson School of Engineering and Applied Sciences,
Harvard University, Cambridge, Massachusetts 02138, USA*

²*Research Laboratory of Electronics, Massachusetts Institute of Technology, Cambridge, Massachusetts 01239, USA*

³*Department of Physics, University of Texas at Austin, Austin, Texas 78712, USA*

⁴*Division of Physics, Mathematics and Astronomy, and Alliance for Quantum Technologies (AQT),
California Institute of Technology, Pasadena, California 91125, USA*

⁵*Department of Physics, Harvard University, Cambridge, Massachusetts 02138, USA*

⁶*Department of Applied Physics, Yale University, New Haven, Connecticut 06520, USA*

(Dated: May 26, 2022)

Acoustic waves at microwave frequencies have been widely used in signal processing applications. They are also emerging as a promising approach for communication and manipulation of quantum information. However, dynamic control of acoustic waves in a low-loss and scalable manner remains an outstanding challenge, which hinders the development of phononic integrated circuits. Here we demonstrate electrical control of traveling acoustic waves on an integrated lithium niobate platform at both room and cryogenic temperatures. We electrically tune the material elasticity to modulate the phase and amplitude of the acoustic waves and demonstrate an acoustic frequency shifter by serrodyne phase modulation. Furthermore, we show reconfigurable nonreciprocal modulation by tailoring the phase matching between acoustic and quasi-traveling electric fields. Our scalable electro-acoustic platform comprises the fundamental elements for arbitrary acoustic signal processing and manipulation of phononic quantum information.

Acoustic waves in solids are the basis for numerous signal processing applications [1] including microwave filters, delay lines, and sensors. Furthermore, they can be used to provide an interface between quantum systems such as superconducting circuits [2–8], defect centers [9, 10], and optical devices [11–15]. Compared to electromagnetic waves, acoustic waves feature five-orders-of-magnitude shorter wavelength and do not radiate into free-space. This therefore allows coherent information processing and manipulation in an ultra-compact footprint with negligible crosstalk between devices and with the environment. For these reasons, on-chip phononic systems have emerged as a promising candidate for quantum computing and storage [15–17]. A phononic integrated circuit requires a few essential functionalities, including efficient transduction from and to electromagnetic waves at microwave frequencies, low-loss waveguiding and routing of acoustic waves, and, importantly, active control of the phase and amplitude of traveling acoustic waves with low energy consumption. The latter is especially important for low-temperature applications. Further, nonreciprocal acoustic isolators and circulators are needed for source protection, bi-directional communication, and noise mitigation. While significant efforts have been made to realize passive phononic integrated circuits and transducers, efficient modulation and isolation of acoustic waves have not been demonstrated, hindering the development of scalable phononic integrated circuits.

Acoustic waveguides on chip have been realized using suspended structures [18, 19], including two-dimensional phononic crystals [20], and high acoustic velocity substrates [21, 22]. Efficient transduction between traveling acoustic waves and electromagnetic waves have also been demonstrated, leveraging piezoelectric coupling with microwaves [18, 19, 21, 22] and optomechanical coupling with light [20]. Controlling the amplitude and phase of an on-chip acoustic wave, on the other hand, has proven to be more challenging since it requires changes in the material elasticity. Previously explored approaches based on, for example, acoustic four-wave mixing [21] and nonlinear mechanical cavities [19], were inefficient and required large acoustic powers due to the weak nonlinearity in the elastic response of most materials. On the other hand, strategies used to achieve acoustic nonreciprocity based on nonlinear materials [23], circulating fluids [24], water-submerged phononic crystals [25], deformed water-air interfaces [26], and optomechanics [27], were all limited to acoustic frequencies below a few megahertz, which renders them unsuitable for applications that require microwave acoustic frequencies. Recent demonstrations of nonreciprocal microwave phonon transmission based on electric amplifiers [28] and semiconductor acoustoelectric effects [29] are not suitable for applications in quantum information processing. Furthermore, approaches using ferromagnetic materials [30] require a magnetic field and therefore are not compatible with quantum technologies that rely on superconducting circuits or spins in solids.

Here we demonstrate electrical control of the fundamental degrees of freedom of acoustic waves at microwave frequencies – their phase and amplitude – using an integrated lithium niobate (LN) electro-acoustic platform.

* shaolb@seas.harvard.edu

† loncar@seas.harvard.edu

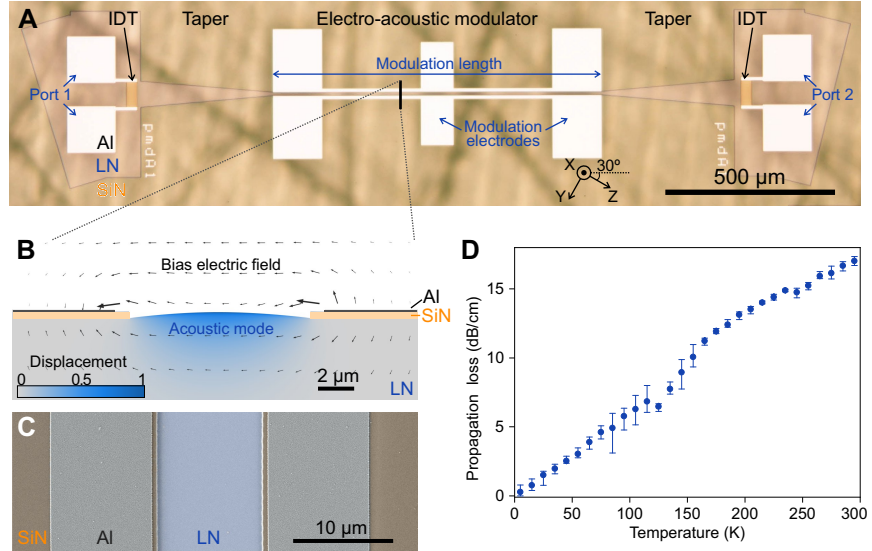


FIG. 1. Lithium niobate (LN) electro-acoustic platform. (A) Optical micrograph of a fabricated device. Bright regions are aluminum (Al). The etched silicon nitride (SiN) layer showing dark boundaries is used to define the acoustic waveguide and regions where the interdigital transducers (IDT) are fabricated. IDTs are used to excite and detect the acoustic waves. The device is on an X-cut LN substrate, and the acoustic waveguide is at 30° angle with respect to the crystal Z-axis (coordinates indicated). The out-of-focus dark lines are scratches on the back side of the chip, which do not affect the device. (B) Cross-section of the acoustic waveguide in the modulation region. The normalized displacement field intensity (blue shading) shows the simulated fundamental acoustic mode. The displacement field is exaggerated for visualization. Arrows indicate the simulated electric field direction and magnitude due to a bias voltage on the modulation electrodes. (C) False-colored scanning electron microscope image of the acoustic waveguide. (D) Measured propagation loss of the acoustic waveguide as a function of temperature.

Furthermore, we utilize these devices to shift the frequency of propagating microwave phonons, and to realize nonreciprocal phase modulation using quasi-traveling electric fields. Modulation of the acoustic waves are enabled by the electro-acoustic effect [31], which is equivalent to electro-optic effect widely utilized to control the phase and amplitude of optical signals. Electro-acoustic effect describes the change in the elasticity of a solid due to an applied electric field, which results in a change of the phase velocity of traveling acoustic waves. The electro-acoustic effect is characterized by the third-order piezoelectric tensor d . The change of elastic constants Δc due to the applied electric field E is given by $\Delta c_{ij} = d_{kij}E_k$, where i, j, k can take values of 1 to 3, corresponding to crystal X, Y and Z directions, and d_{kij} is subject to the material symmetry [32]. However, since this electro-acoustic effect is relatively weak, bulk components show small phase changes [31] and are unsuitable for practical applications. Here we overcome this limitation by confining the acoustic wave to a wavelength-scale acoustic waveguide and placing the modulation electrodes closely across the waveguide, allowing π -phase shift to be achieved.

Our electro-acoustic modulators are fabricated on an X-cut LN substrate (Fig. 1A), where we employ the third-

order piezoelectric coefficients of LN by using guided acoustic modes and applying electric fields mainly in the Y direction. The acoustic waveguide is formed by creating a 10 μm slot inside thin silicon nitride (SiN) film deposited on top of LN (Figs. 1B and 1C). Since the acoustic velocity (index) of SiN is greater (smaller) than that of LN, an acoustic mode is confined (Fig. 1B). We note that our waveguide supports a Rayleigh-type acoustic wave [1] with most of its strain field in the XZ component. Inter-digital transducers (IDT) are used to electrically excite and detect microwave acoustic waves. The pitch of the IDT finger electrodes is 650 nm and equal to the half wavelength of the acoustic waves at 2.5 GHz. To optimize the transduction efficiency, the width of the IDT (75 μm) is designed to be larger than the acoustic waveguide (10 μm), and tapered waveguide structures are used to couple the wave into the acoustic waveguide. Importantly, the waveguide is oriented along 30° angle with respect to the crystal Z axis, as this direction features the smallest acoustic velocity on the X-cut surface and thus provides the best acoustic wave confinement (Fig. S1). Finally, aluminum (Al) electrodes are deposited on the SiN layer and used to apply the electric field needed for acoustic index modulation.

Low loss is critical for realizing large-scale phononic in-

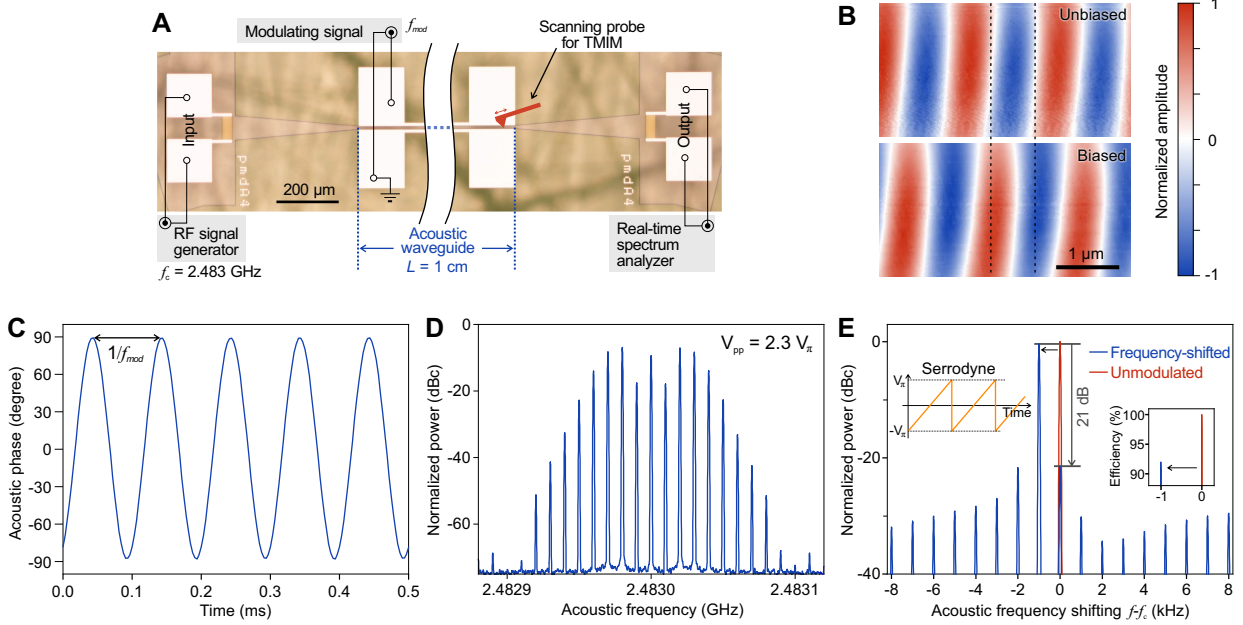


FIG. 2. Electro-acoustic phase modulation. (A) Experimental setup for characterizing the electro-acoustic phase modulator. A signal generator is used to excite the acoustic wave via an IDT at carrier frequency $f_c = 2.483$ GHz. A modulating signal with frequency f_{mod} is applied to the modulation electrodes, and a real-time spectrum analyzer is used to detect the phase and amplitude of transmitted acoustic signal detected by an identical IDT. In the transmission-mode microwave impedance microscopy (TMIM), a scanning probe is used to detect the acoustic field. (B) TMIM images show phase shift of the acoustic wave due to an applied bias voltage on the modulation electrodes. The scanning region is located at the center of the waveguide near the output of the modulator. (C) Phase of the transmitted acoustic wave measured by the real-time spectrum analyzer when the modulator is driven by a $f_{\text{mod}} = 10$ kHz sine wave with peak-to-peak voltage $V_{\text{pp}} = 53$ V, showing full 180° phase oscillation. This indicates a half-wave voltage $V_\pi = 53$ V. (D) By driving the phase modulator harder, additional acoustic sidebands can be generated, resulting in formation of an electro-acoustic frequency comb. Here, an $f_c = 2.483$ GHz acoustic wave is modulated by a 10 kHz sine wave with $V_{\text{pp}} = 2.3V_\pi$. (E) Serrodyne frequency shift of an acoustic wave by 1 kHz. This is achieved by applying a repeating linear voltage ramp (serrodyne) with $V_{\text{pp}} = 2V_\pi$ (Left inset). Right inset plots the acoustic powers in a linear scale, showing an efficiency of 92%. The spectral powers in (D) and (E) are normalized to the unmodulated signal received by the spectrum analyzer. The results shown in this figure are measured from the same device with a modulation length of 1 cm.

egrated circuits. We measure the propagation loss of the acoustic waveguide [32] at different temperatures down to 1 K (Fig. 1D). At room temperature (300 K) and under vacuum, the acoustic propagation loss is $\alpha = 17$ dB/cm. It decreases with lowered temperature to $\alpha = 5$ dB/cm at liquid nitrogen temperature (77 K) and < 1 dB/cm at 1.3 K. These values are consistent with those measured using acoustic cavities on LN [21, 33]. Thermoelastic dissipation [34] is the likely source of loss at temperatures above 1 K.

Next, we measure the performance of a 1-cm-long electro-acoustic phase modulator by inputting an acoustic wave at carrier frequency $f_c = 2.483$ GHz and detecting phase and amplitude of the modulated acoustic wave (Fig. 2A). The insertion loss of the device, measured from a microwave signal applied to one IDT and detected after the other, is 10 dB at 1.3 K. This loss is dominated by the symmetric IDTs that excite and collect acoustic waves bidirectionally, which result in a 3 dB loss at each IDT,

and the tapers that guide acoustic waves to the waveguide. At room temperature, the insertion loss increases by 25 dB due to higher propagation loss and a lower efficiency of IDTs (Fig. S2). We used transmission-mode microwave impedance microscopy (TMIM), a scanning probe technique that coherently measure the profiles of traveling acoustic waves near the output of the modulator waveguide [32]. We observe a $\pi/2$ phase shift of the acoustic wave when a 50 V DC bias voltage is applied to the modulation electrode (Fig. 2B). This measurement of the traveling wave profile confirms that the acoustic wave is being directly modulated.

To measure the half-wave voltage V_π of the modulator, we apply a sinusoidal signal at $f_{\text{mod}} = 10$ kHz on the phase modulator electrode and analyze the output by a real-time spectrum analyzer. The phase change increases linearly with the amplitude of modulating signal (Fig. S3). When the peak-to-peak voltage (V_{pp}) of the modulating signal reaches 53 V, a π -phase change

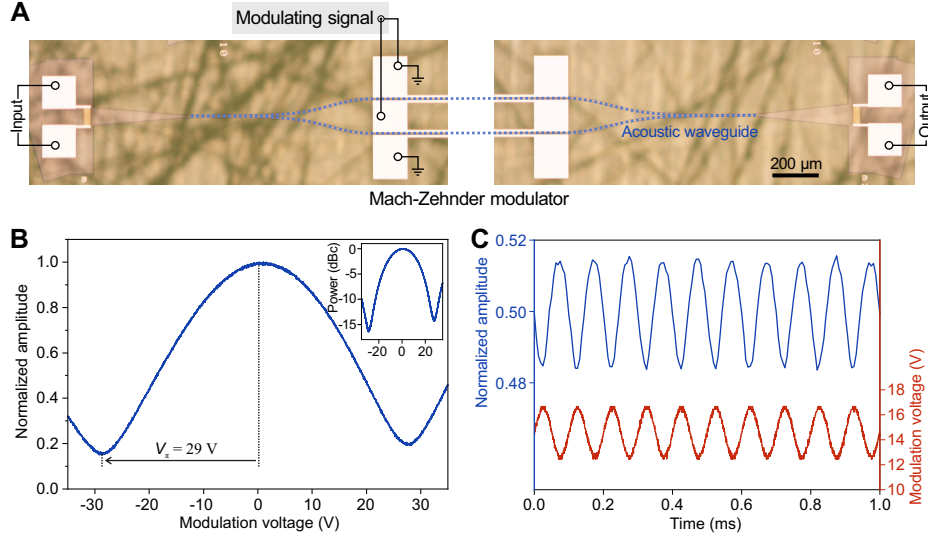


FIG. 3. Electro-acoustic amplitude modulation. (A) Schematic of the electro-acoustic Mach-Zehnder modulator. The modulating signal is applied at the middle electrode while two outer electrodes are ground, and thus two acoustic waveguides experience electric fields with opposite polarities. (B) Measured output acoustic amplitude (main figure) and power (Inset) with slowly varying modulating voltage to determine the V_π of the modulator. (C) Measured acoustic amplitude with a weak modulating signal at $f_{mod} = 10$ kHz and biased at $0.5V_\pi$.

of the received acoustic wave is observed at room temperature (Fig. 2C), inferring a $V_\pi = 53$ V. At 1.3 K, the peak transmission frequency shifts to 2.532 GHz, and the V_π increases to 133 V (Fig. S3). An important figure of merit for the modulator, the product between its half-wave voltage V_π , length L , and propagation loss α , i.e., $V_\pi L \alpha$, is reduced by a factor of 7 (from 900 V·dB to 120 V·dB) at 1.3 K owing to reduced propagation loss compared to room temperature. The V_π of the phase modulator could be further reduced by a factor of 2 by using narrower acoustic waveguides, which is possible using materials with higher acoustic contrast. In addition, we measure the 3-dB bandwidth to be 110 kHz and observe zero modulation at $f_{mod} = 336$ kHz when the period of the modulating signal matches the traveling time of the acoustic wave (Fig. S4).

We demonstrate two proof-of-concept applications – electro-acoustic frequency comb and acoustic frequency shifting. By driving the phase modulator with a 10 kHz sinusoidal signal of $V_{pp} = 2.3V_\pi$, we generate 19 equidistant frequency comb lines centered at $f_c = 2.483$ GHz (Fig. 2D). The frequency comb coherently generates new frequencies and may become useful for short acoustic pulse generations and frequency domain information processing. Additionally, the ability to modulate over a full 2π phase allows us to demonstrate acoustic frequency shifting using a serrodyne approach. Specifically, by applying a repeating linear voltage ramp signal at the frequency of 1 kHz with V_{pp} of $2V_\pi$, the modulated acoustic wave experiences an approximately linear phase ramp in time, which results in change (shift) in frequency of the acoustic wave. We measure shift efficiency of 92%

(Fig. 2E), defined as the ratio of detected acoustic power at the shifted frequency and the power of unmodulated acoustic wave. The carrier suppression of our frequency shifter is 21 dB.

We realize amplitude modulation of acoustic wave by constructing an acoustic Mach-Zehnder interferometer (MZI) in the push-pull configuration (Fig. 3A). The input acoustic wave is split equally between two MZI arms, and the two waves experience different phase shifts as they propagate in each arm. The phase difference is controlled by the voltage applied to the electrodes. When the two waves recombine, the acoustic interference yields an amplitude modulation. Maximum output amplitude occurs when the phase difference between the two paths is zero (no voltage applied) or an even integer number of π , while the minimum amplitude occurs when the phase difference is an odd integer number of π . We measure $V_\pi = 29$ V at quasi-DC frequency for an 8-mm-long acoustic Mach-Zehnder modulator. The extinction ratio between the maximum and minimum output power is over 15 dB (Fig. 3B), which could be limited by the fabrication imperfection of the Y-splitter or the existing of higher order modes of the waveguide. When the modulator is biased to the quadrature point (i.e., 50% transmission), the amplitude of the output acoustic waves follows the small input signal accordingly (Fig. 3C).

To achieve nonreciprocal transmission of acoustic waves, we employ a quasi-travelling electric field to break the symmetry of counter-propagating acoustic waves. By separating modulation electrode into three segments, we can control the wave number (momentum) of the quasi-travelling electric field by adjusting the relative phase of

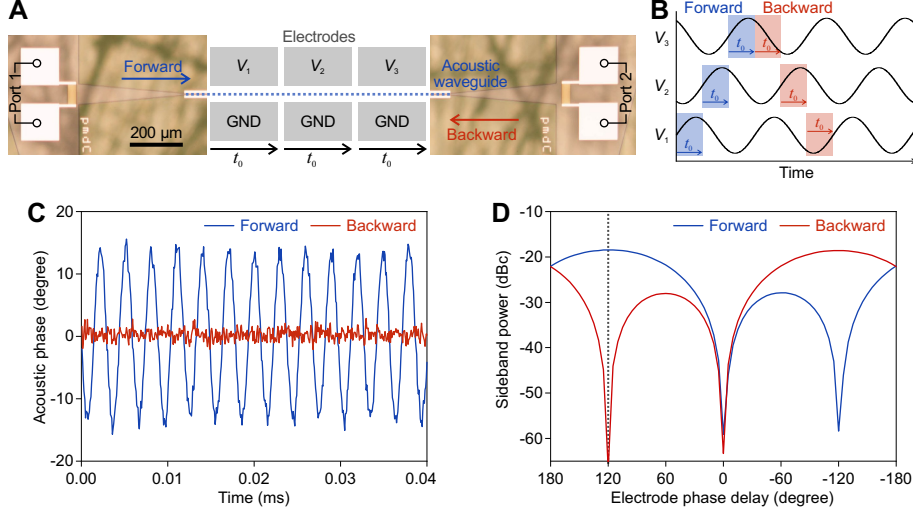


FIG. 4. **Nonreciprocal phase modulation of acoustic waves.** (A) Schematic of the device used for nonreciprocal phase modulation. The modulation electrode is separated into three segments with independently controlled voltage V_1 to V_3 . The acoustic traveling time through each segment is t_0 . (B) Illustration of nonreciprocal modulation of forward and backward propagating acoustic waves. The voltage applied on each segment of the electrodes is progressively delayed by 120° . For forward traveling acoustic wave, the phase accumulated in each segment is the same and results in net modulation. For backward traveling acoustic wave, the accumulated phase in each segment is different and can be designed to result in a net zero phase shift. (C) Measured acoustic phases acquired for both forward and backward propagating acoustic waves. (D) Measured modulation sideband power of the forward and backward propagating acoustic waves for varying phase delays between the voltages applied to the electrodes. The dashed line indicates the operating condition in (C) and a > 40 dB nonreciprocity. The modulation frequency is $f_{mod} = 1/(3t_0) = 336$ kHz in (C) and (D).

modulating signals applied to each electrode (Fig. 4A). This approach enables nonreciprocal acoustic phase modulation when the quasi-traveling modulating signal is phase matched with the traveling acoustic wave in one direction but mismatched with that in the opposite direction (Fig. 4B and Movie S1). Maximum nonreciprocity occurs when the signals applied to each succeeding modulation electrode segments are phase delayed by 120° and when the modulation frequency matches the total traveling time of the acoustic wave, i.e., $1/f_{mod} = 3t_0$, where t_0 is the time for acoustic wave to travel through one electrode segment. In this case, the forward propagating acoustic wave always experiences the same phase modulation when it traverses the electrodes and thus results in maximum modulation. On the other hand, the backward propagating wave effectively experiences a full (2π) modulation cycle, which results in no net phase change. To implement this concept, we fabricate such a nonreciprocal acoustic modulator with 1 cm length and apply the required modulation frequency $f_{mod} = 1/(3t_0) = 336$ kHz for maximum nonreciprocity. At this condition, we observe the presence (absence) of acoustic phase modulations in the forward (backward) propagation direction (Fig. 4C).

The acoustic nonreciprocity can be adjusted by the relative phase of the signals applied to the modulation electrodes (Fig. 4D). We observe a maximum nonreciprocity

of over 40 dB of the modulation sideband power. Furthermore, we sweep the modulation frequency and the phase delay between the applied voltages on the three electrodes, and clearly observe maximum modulation sideband powers when the traveling acoustic wave and the modulating signal are phase-matched, and zero modulation when they are phase mismatched by any positive integer number of 2π phases (Fig. S5). With additional filters and couplers, we could build acoustic isolators and circulators based on our frequency shifter and nonreciprocal phase modulator.

In conclusion, we demonstrate an integrated electro-acoustic platform that provides arbitrary control of on-chip traveling acoustic waves, namely their phase and amplitude. Compared with approaches based on optomechanics and nonlinear acoustics, our electro-acoustic modulators show significant advantages in terms of modulation efficiency, simplicity in fabrication, and scalability. Taken together, these advantages may enable realization of large scale integrated acoustic information processing systems. Using advanced nanofabrication, we could push the operation frequency of our device to tens of GHz, covering the 5G millimeter wave bands. We expect the half-wave voltage V_π to decrease quadratically with higher frequency, as both the width of the acoustic waveguide and the acoustic wave number scale linearly with frequency. Our devices may find applications in

emerging acoustically mediated quantum networks that allow connecting different solid-state systems and thus may enable hybrid quantum networks that leverage the distinct functionalities of each system for quantum computing, communication and sensing [35]. In particular, phase modulation is necessary for control of coherent interactions and entanglement between solid state systems, dynamical routing and synchronization for addressability and error mitigation, compensating environmental changes such as local temperature drifts, or for compensating unavoidable detuning between quantum systems. Finally, our devices offer an opportunity to build versatile acoustic signal processing components, such as, tunable filters and reconfigurable duplexers, which would minimize the number of acoustic components for next-generation telecommunications.

ACKNOWLEDGMENTS

We thank Prof. Cheng Wang and Cleaven Chia for fruitful discussion. **Funding:** This work is supported by ONR QOMAND grant no. N00014-15-1-2761, DOE

HEADS-QON grant no. DE-SC0020376, NSF grant no. DMR-2004536, the Welch Foundation Grant F-1814, and NSF RAISE/TAQS grant no. ECCS-1839197. N.S. is supported by the Natural Sciences and Engineering Research Council of Canada (NSERC), the AQT Intelligent Quantum Networks and Technologies (INQNET) research programme and the DOE/HEP QuantISED programme grant and DOE award no. DE-SC0019219. **Author contributions:** L.S.: Conceptualization, Methodology, Investigation, Formal analysis, Visualization, Writing - Original Draft. D.Z.: Methodology, Investigation, Writing - Original Draft. M.C.: Investigation, Writing - Review & Editing. D.H.L.: Investigation, Writing - Review & Editing. N.S.: Writing - Original Draft. Y.H.: Writing - Review & Editing. P.T.R.: Writing - Review & Editing. K.L.: Resources, Methodology, Writing - Review & Editing, Supervision. K.K.B.: Resources, Writing - Review & Editing, Supervision. M.L.: Resources, Writing - Review & Editing, Supervision. **Competing interests:** M.L. is involved in developing lithium niobate technologies at HyperLight Corporation. The other authors declare no competing interests.

[1] C. Campbell, *Surface Acoustic Wave Devices and their Signal Processing Applications* (Academic Press, San Diego, CA, 1989) pp. 31–57.

[2] Y. Chu, P. Kharel, W. H. Renninger, L. D. Burkhardt, L. Frunzio, P. T. Rakich, and R. J. Schoelkopf, *Science* **358**, 199 (2017).

[3] R. Manenti, A. F. Kockum, A. Patterson, T. Behrle, J. Rahamim, G. Tancredi, F. Nori, and P. J. Leek, *Nat Commun* **8**, 975 (2017).

[4] K. J. Satzinger, Y. P. Zhong, H. S. Chang, G. A. Peairs, A. Bienfait, M. H. Chou, A. Y. Cleland, C. R. Conner, E. Dumur, J. Grebel, I. Gutierrez, B. H. November, R. G. Povey, S. J. Whiteley, D. D. Awschalom, D. I. Schuster, and A. N. Cleland, *Nature* **563**, 661 (2018).

[5] P. Arrangoiz-Arriola, E. A. Wollack, Z. Wang, M. Pechal, W. Jiang, T. P. McKenna, J. D. Witmer, R. Van Laer, and A. H. Safavi-Naeini, *Nature* **571**, 537 (2019).

[6] A. Bienfait, K. J. Satzinger, Y. P. Zhong, H.-S. Chang, M.-H. Chou, C. R. Conner, E. Dumur, J. Grebel, G. A. Peairs, R. G. Povey, and A. N. Cleland, *Science* **364**, 368 (2019).

[7] G. Andersson, B. Suri, L. Guo, T. Aref, and P. Delsing, *Nature Physics* **15**, 1123 (2019).

[8] M. V. Gustafsson, T. Aref, A. F. Kockum, M. K. Ekström, G. Johansson, and P. Delsing, *Science* **346**, 207 (2014).

[9] S. J. Whiteley, G. Wolfowicz, C. P. Anderson, A. Bourassa, H. Ma, M. Ye, G. Koolstra, K. J. Satzinger, M. V. Holt, F. J. Heremans, A. N. Cleland, D. I. Schuster, G. Galli, and D. D. Awschalom, *Nature Physics* **15**, 490–495 (2019).

[10] S. Maity, L. Shao, S. Bogdanović, S. Meesala, Y.-I. Sohn, N. Sinclair, B. Pingault, M. Chalupnik, C. Chia, L. Zheng, K. Lai, and M. Lončar, *Nature Communications* **11**, 193 (2020).

[11] W. Jiang, C. J. Sarabalis, Y. D. Dahmani, R. N. Patel, F. M. Mayor, T. P. McKenna, R. Van Laer, and A. H. Safavi-Naeini, *Nature Communications* **11**, 1166 (2020).

[12] L. Shao, M. Yu, S. Maity, N. Sinclair, L. Zheng, C. Chia, A. Shams-Ansari, C. Wang, M. Zhang, K. Lai, and M. Lončar, *Optica* **6**, 1498 (2019).

[13] B. J. Eggleton, C. G. Poulton, P. T. Rakich, M. J. Steel, and G. Bahl, *Nature Photonics* **13**, 664 (2019).

[14] M. Forsch, R. Stockill, A. Wallucks, I. Marinković, C. Gärtner, R. A. Norte, F. van Otten, A. Fiore, K. Srinivasan, and S. Gröblacher, *Nature Physics* **16**, 69 (2020).

[15] G. S. MacCabe, H. Ren, J. Luo, J. D. Cohen, H. Zhou, A. Sipahigil, M. Mirhosseini, and O. Painter, *Science* **370**, 840 (2020).

[16] C. T. Hann, C.-L. Zou, Y. Zhang, Y. Chu, R. J. Schoelkopf, S. M. Girvin, and L. Jiang, *Physical Review Letters* **123**, 250501 (2019).

[17] M. Pechal, P. Arrangoiz-Arriola, and A. H. Safavi-Naeini, *Quantum Science and Technology* **4**, 015006 (2018).

[18] Y. D. Dahmani, C. J. Sarabalis, W. Jiang, F. M. Mayor, and A. H. Safavi-Naeini, *Physical Review Applied* **13**, 024069 (2020).

[19] D. Hatanaka, I. Mahboob, K. Onomitsu, and H. Yamaguchi, *Nature Nanotechnol* **9**, 520 (2014).

[20] K. Fang, M. H. Matheny, X. Luan, and O. Painter, *Nature Photonics* **10**, 489 (2016).

[21] F. M. Mayor, W. Jiang, C. J. Sarabalis, T. P. McKenna, J. D. Witmer, and A. H. Safavi-Naeini, arXiv , 2007.04961 (2020).

[22] W. Fu, Z. Shen, Y. Xu, C. L. Zou, R. Cheng, X. Han, and H. X. Tang, *Nature Communications* **10**, 2743 (2019).

[23] B. Liang, X. S. Guo, J. Tu, D. Zhang, and J. C. Cheng,

Nature Materials **9**, 989 (2010).

[24] R. Fleury, D. L. Sounas, C. F. Sieck, M. R. Haberman, and A. Alù, **Science** **343**, 516 (2014).

[25] E. Walker, A. Neogi, A. Bozhko, Y. Zubov, J. Arriaga, H. Heo, J. Ju, and A. A. Krokhin, **Physical Review Letters** **120**, 204501 (2018).

[26] T. Devaux, A. Cebrecos, O. Richoux, V. Pagneux, and V. Tournat, **Nature Communications** **10**, 3292 (2019).

[27] H. Xu, L. Jiang, A. A. Clerk, and J. G. E. Harris, **Nature** **568**, 65 (2019).

[28] L. Shao, W. Mao, S. Maity, N. Sinclair, Y. Hu, L. Yang, and M. Lončar, **Nature Electronics** **3**, 267 (2020).

[29] H. Mansoorzare and R. Abdolvand, **IEEE Electron Device Letters** **41**, 1444 (2020).

[30] T. Nomura, X. X. Zhang, S. Zherlitsyn, J. Wosnitza, Y. Tokura, N. Nagaosa, and S. Seki, **Physical Review Letters** **122**, 145901 (2019).

[31] Y. Cho and K. Yamanouchi, **Journal of Applied Physics** **61**, 875 (1987).

[32] See Supplemental Materials for additional data, experimental details, and descriptions.

[33] L. Shao, S. Maity, L. Zheng, L. Wu, A. Shams-Ansari, Y.-I. Sohn, E. Puma, M. N. Gadalla, M. Zhang, C. Wang, E. Hu, K. Lai, and M. Lončar, **Physical Review Applied** **12**, 014022 (2019).

[34] S. K. De and N. R. Aluru, **Physical Review B** **74**, 144305 (2006), pRB.

[35] G. Kurizki, P. Bertet, Y. Kubo, K. Mølmer, D. Petrosyan, P. Rabl, and J. Schmiedmayer, **Proceedings of the National Academy of Sciences** **112**, 3866 (2015).

[36] L. Zheng, D. Wu, X. Wu, and K. Lai, **Physical Review Applied** **9**, 061002 (2018).

[37] L. Zheng, L. Shao, M. Loncar, and K. Lai, **IEEE Microwave Magazine** **21**, 60 (2020).

Supplemental Materials: Electrical Control of Surface Acoustic Waves

I. DESIGN OF THE ELECTRO-ACOUSTIC MODULATORS

The interdigital transducers (IDTs) are optimized for maximum transduction between acoustic and electrical waves at 2.5 GHz. The aperture of the IDT is $75\ \mu\text{m}$, the pitch of the finger electrode is 650 nm, and the number of finger electrode pairs per IDT is 25. The maximum transmission between two IDTs at 2.5 GHz is -8 dB at room temperature, with -6 dB resulting from the symmetric design of the IDTs (-3 dB per IDT). The adiabatic taper that connects an IDT to an acoustic waveguide is 400 μm long. The insertion loss per acoustic taper is about 5 dB at room temperature, as extracted from the measured transmission of devices with and without the tapered structure. An X-cut lithium niobate (LN) substrate is used for all devices. The direction of the acoustic waveguide is at an angle of 30° with respect to the crystal Z-axis (Fig. 1A). This direction features the slowest surface acoustic wave phase velocity using X-cut LN and thus leads to a well-confined acoustic mode for the waveguide (Fig. S1). The modulating electric field applied across the waveguide is mainly in the crystal Y-direction. As most strain field of the guided acoustic mode is in the XZ component (corresponding to index 5 in the Voigt notation), our device employs a non-zero electro-acoustic modulation coefficient d_{255} .

II. DEVICE FABRICATION

A 400 nm-thick silicon nitride (SiN) layer is deposited by plasma enhanced chemical vapor deposition on the X-cut LN substrate. The SiN layer is patterned by a direct write lithography tool (Heidelberg Instruments MLA150) and etched by reactive ion etching using carbon tetrafluoride (CF₄), sulfur hexafluoride (SF₆) and hydrogen (H₂) gases. The metal layer is patterned by an electron lithography tool (Elionix ELS-F125) using polymethyl methacrylate (PMMA) resist. A 115 nm-thick layer of aluminum is deposited by an electron beam evaporation tool, and lift-off in a 1-methyl-2-pyrrolidone (NMP) solvent for more than 3 hours at 80 °C.

III. DEVICE MEASUREMENTS

The devices are mounted and wire-bonded to a printed circuit board (PCB). The transmission spectra of the devices are measured using a vector network analyzer (Keysight N5224A). For the modulation experiments, a microwave signal generator drives one IDT using a single-frequency tone around 2.5 GHz, and a real-time spectrum analyzer (RSA) is connected to the other IDT. The RSA not only measures the power spectrum of the acoustic wave received by the IDT, but also demodulates the signal to provide real-time in-phase and quadrature data, which are converted to the phase and amplitude of the received signal. The microwave signal generator and the RSA are synchronized by a 10 MHz clock. An arbitrary waveform generator is used to provide any low-frequency modulation signals, and a 20 kHz-bandwidth voltage amplifier (Falco Systems, WMA-005) is used to provide a 20 times amplification in voltage up to $\pm 75\ \text{V}$ when necessary. For nonreciprocal phase modulation, a four-channel arbitrary waveform generator (Tabor WS8104A-DST) is used to generate the three synchronized modulation signals with various phase delays.

IV. LOW-TEMPERATURE SETUP

The low-temperature performance of the device is measured in a closed-cycle cryostat (ICE Oxford) that reaches a base temperature of $\sim 0.8\ \text{K}$. The temperature, transmission (S_{21}), and half-wave voltage of the devices are monitored continuously as the cryostat cools from room temperature. These measurements are repeated as the cryostat warms up. Cable losses are independently calibrated during a separate cooldown. To characterize the propagation loss of the SAWs, the transmission of two acoustic waveguides with different lengths is measured and compared. These waveguides are fabricated on the same chip, packaged on the same PCB, and connected using identical cables.

V. TRANSMISSION-MODE MICROWAVE IMPEDANCE MICROSCOPY

The acoustic-wave profiles in the main text are directly imaged using the transmission-mode microwave impedance microscopy (TMIM) [36, 37], which is implemented on a commercial atomic-force microscopy (AFM) platform ParkAFM XE-70. Here the IDT is driven by a continuous microwave input signal (Anritsu MG 3692A), which

launches the propagating surface acoustic wave. During the AFM scanning, the customized cantilever probe from PrimeNano Inc. picks up the GHz piezoelectric potential accompanying the acoustic wave. By using the same excitation frequency as the reference, the TMIM electronics demodulate the tip signal into a time-independent spatial pattern that is shown in Fig. 2B. Note that the TMIM image contains information on the phase of the propagating wave [37]. As a result, a lateral shift of the wave pattern indicates that the acoustic wave is modulated by the DC bias electric field. Due to the charging effects at interfaces between layers, a higher DC bias voltage is required to achieve same phase shift than that of a modulating signal at $f_{mod} = 10$ kHz.

VI. ELECTRO-ACOUSTIC EFFECT

Hooke's law says that the force on a spring is proportional to its displacement. The square of the resonant frequency of a mass-spring system is equal to the ratio of the spring proportionality constant to the mass. Thus, tuning the spring constant also varies the resonance frequency of the spring.

Weakly-excited acoustic waves in solids follow a generalized Hooke's law that relates stress σ and strain ϵ by an elasticity (stiffness) matrix \mathbf{C} , which is a 6-by-6 matrix in Voigt notation. LN is of point group 3m, which has a three-fold rotation symmetry about its Z axis and mirror symmetry on its X axis. With vanishing components of \mathbf{C} due to the symmetry of LN, the relation is

$$\begin{bmatrix} \sigma_1 \\ \sigma_2 \\ \sigma_3 \\ \sigma_4 \\ \sigma_5 \\ \sigma_6 \end{bmatrix} = \begin{bmatrix} c_{11} & c_{12} & c_{13} & c_{14} & 0 & 0 \\ c_{12} & c_{11} & c_{13} & -c_{14} & 0 & 0 \\ c_{13} & c_{13} & c_{33} & 0 & 0 & 0 \\ c_{14} & -c_{14} & 0 & c_{44} & 0 & 0 \\ 0 & 0 & 0 & 0 & c_{44} & c_{14} \\ 0 & 0 & 0 & 0 & c_{14} & \frac{1}{2}(c_{11} - c_{12}) \end{bmatrix} \begin{bmatrix} \epsilon_1 \\ \epsilon_2 \\ \epsilon_3 \\ \epsilon_4 \\ \epsilon_5 \\ \epsilon_6 \end{bmatrix}.$$

The elasticity matrix of LN can be varied by an applied electric field, $\Delta c_{ij} = d_{kij}E_k$, where $i,j=1\cdot 6$, $k = 1, 2, 3$, \mathbf{E} is the applied electric field, and \mathbf{D} (d_{kij}) is the third-order piezoelectric tensor. Subject to the symmetry of LN, \mathbf{D} has the following form,

$$\begin{aligned} d_{1ij} &= \begin{bmatrix} 0 & 0 & 0 & 0 & d_{115} & d_{116} \\ 0 & 0 & 0 & 0 & d_{125} & d_{126} \\ 0 & 0 & 0 & 0 & d_{135} & d_{136} \\ 0 & 0 & 0 & 0 & d_{145} & \frac{1}{2}(d_{115} - d_{125}) \\ d_{115} & d_{125} & d_{135} & d_{145} & 0 & 0 \\ d_{116} & d_{126} & d_{136} & \frac{1}{2}(d_{115} - d_{125}) & 0 & 0 \end{bmatrix} \\ d_{2ij} &= \begin{bmatrix} \frac{1}{2}(d_{116} + 3d_{126}) & \frac{1}{2}(d_{116} - d_{126}) & d_{136} & d_{125} & 0 & 0 \\ \frac{1}{2}(d_{116} - d_{126}) & -\frac{1}{2}(3d_{116} + d_{126}) & -d_{136} & d_{115} & 0 & 0 \\ d_{136} & -d_{136} & 0 & d_{135} & 0 & 0 \\ d_{125} & d_{115} & d_{135} & -d_{145} & 0 & 0 \\ 0 & 0 & 0 & 0 & d_{145} & \frac{1}{2}(d_{115} - d_{125}) \\ 0 & 0 & 0 & 0 & \frac{1}{2}(d_{115} - d_{125}) & \frac{1}{2}(d_{116} - d_{126}) \end{bmatrix} \\ d_{3ij} &= \begin{bmatrix} d_{311} & d_{312} & d_{313} & d_{314} & 0 & 0 \\ d_{312} & d_{311} & d_{313} & -d_{314} & 0 & 0 \\ d_{313} & d_{313} & d_{333} & 0 & 0 & 0 \\ d_{314} & -d_{314} & 0 & d_{344} & 0 & 0 \\ 0 & 0 & 0 & 0 & d_{344} & d_{314} \\ 0 & 0 & 0 & 0 & d_{314} & \frac{1}{2}(d_{311} - d_{312}) \end{bmatrix}. \end{aligned}$$

VII. COUPLING BETWEEN A TRAVELING ACOUSTIC WAVE AND A BIAS ELECTRIC FIELD

An applied electric field affects the traveling acoustic wave by tuning the elasticity of the material. When the applied electric field is small, such tuning in elasticity can be treated by the perturbation theory. The wave equation for a guided acoustic mode is

$$-\rho\omega^2 \mathbf{u} = \nabla \bullet (\mathbf{C} \epsilon),$$

where ρ is the mass density of the material, \mathbf{u} is the displacement field, ω is the angular frequency of the eigenmode at given wavenumber k .

For a guided acoustic mode, the first-order shift in the eigenfrequency at the given wavenumber k due to the perturbation of elasticity $\Delta\mathbf{C}$ is given by

$$\frac{\Delta\omega}{\omega} = \frac{\int dr \Delta c_{ij} \epsilon_i^* \epsilon_j}{2 \int dr c_{ij} \epsilon_i^* \epsilon_j} = \frac{\int dr d_{kij} E_k \epsilon_i^* \epsilon_j}{2 \int dr c_{ij} \epsilon_i^* \epsilon_j}.$$

The integral is over the whole cross section that perpendicular to the acoustic propagation direction. Further, the change of wavenumber Δk at certain mode frequency ω is calculated by the dispersion relation of the acoustic mode,

$$\frac{\Delta k}{k} = \frac{\Delta\omega}{\omega} \frac{v_p}{v_g},$$

where v_p and v_g are the phase and group velocity of the guided acoustic mode. The overall acoustic phase change over length L due to the applied electric field is $\Delta k L$.

VIII. MEASUREMENT OF THE MODULATION BANDWIDTH

First, we measure the modulation bandwidth of the 1-cm-long phase modulator (Fig. 2). We apply a weak signal modulation ($V_{pp} = 0.2V_\pi$) with varied frequency and measure the modulation efficiency. The modulation efficiency is indicated by the first sideband power generated by the phase modulation. Due to the phase mismatch between the slowly propagating acoustic wave and the fast varying electrical modulation signals, we measure the 3-dB bandwidth to be 110 kHz for the 1-cm phase modulator and observe periodic variations of the sideband power as a function of modulation frequency (Fig. S4). The modulation efficiency approaches zero every time when the modulation frequency is an integer multiple (N) of $f_{mod} = 336$ kHz. At these frequencies, the electric field oscillates exactly N full cycles as the acoustic wave travels through the modulator, resulting in a vanishing cumulative modulation effect. The zero-modulation frequency is related to the modulation length L and the acoustic group velocity v_g by $f_{mod} = \frac{v_g}{L}$. Using this relationship, we infer an acoustic group velocity of $v_g = 3.36$ km/s, which is consistent with simulated velocity of 3.38 km/s (Fig. S1).

CAPTION FOR MOVIE S1

Principle of nonreciprocal acoustic phase modulation. First (last) 30s depicts a wave-front of the acoustic wave as a blue (red) dot traveling in the forward (backward) direction. Top window illustrates three electrodes of the modulator, labelled as V_1 , V_2 and V_3 , that have sinusoidal signals applied which are 120° out of phase with each other. Bottom window depicts the signals in the time domain, depicting the electrode regions for each signal. Middle window indicates the phase accumulation experienced by the wave-front as it propagates through the modulator.

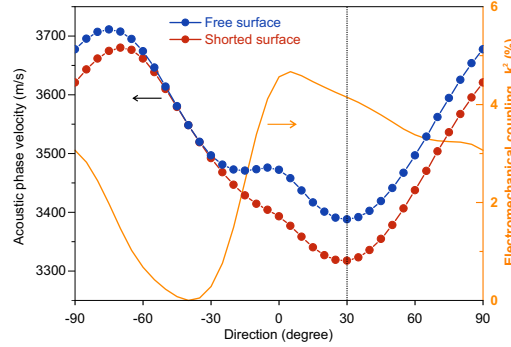


FIG. S1. **Simulated acoustic phase velocities for varying directions on X-cut LN.** The direction is defined by the angle respective to the crystal Z axis. The electromechanical coupling coefficient $k^2 = 2 (v_o - v_m)/v_o$, where v_o and v_m are the phase velocities when the top surface is free and electrically shorted, respectively. The direction of the waveguide used in our device is 30°, as indicated by the dash line.

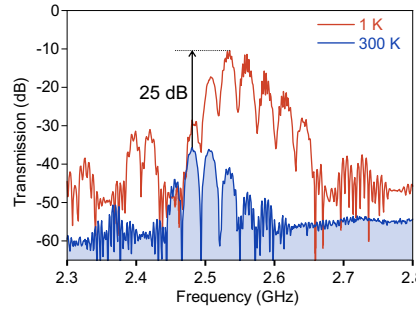


FIG. S2. **Measured transmission spectra of the acoustic modulator at temperatures of 300 and 1.3 K.** The results indicate a 25 dB improvement in peak transmission at low temperature. The frequency shift of the spectrum is due to the temperature dependent elasticity of LN.

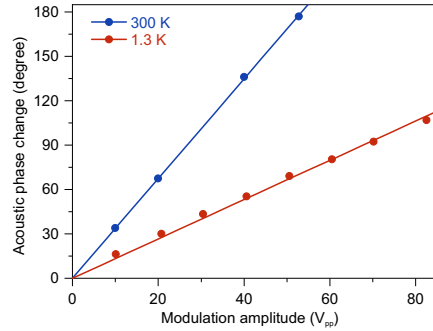


FIG. S3. Peak-to-peak acoustic phase changes due to sinusoidal modulating signals of varying peak-to-peak voltage (V_{pp}) at room and cryogenic temperatures. The sinusoidal modulation signals are of the frequency $f_{mod} = 10$ kHz. Linear fits show V_π of 53 V at room temperature (300 K) and 135 V at 1.3 K, respectively.

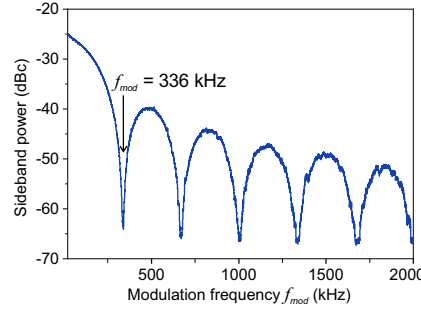


FIG. S4. Modulation bandwidth of the 1-cm-long electro-acoustic phase modulator. The modulation efficiency is indicated by the first sideband power due to the phase modulation. The measured 3-dB bandwidth is 110 kHz. The modulation approaches zero at $f_{mod} = 336$ kHz when the acoustic traveling time through the modulator equals $1/f_{mod}$. The same device is measured as that in Fig. 2.

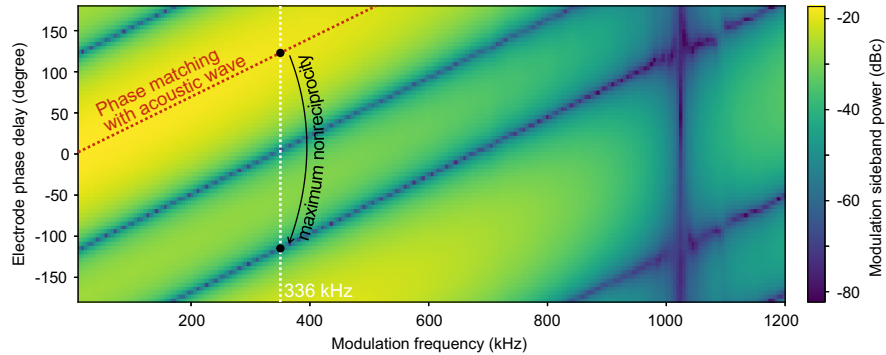


FIG. S5. Phase matching between a traveling acoustic wave and a quasi-traveling electric field. The modulation sideband power is measured with varied modulation frequency and phase delay between the three electrodes. The maximum modulations that satisfy the phase matching condition are indicated by the red line. The condition for the maximum nonreciprocity in phase modulation is indicated by the black dots, as the counter propagating acoustic waves experience opposite phase delays compared to the propagating waves. The sideband power is normalized to the unmodulated carrier acoustic wave power. The measured date is from the same device as in Figs. 4C and 4D, which consists of three electrodes with overall modulation length of 1 cm.